Differential Heating of Metal Nanostructures at Radio Frequencies

Nicholas J. Rommelfanger,[1,2] Zihao Ou,[2,3] Carl H.C. Keck,[2,3] and Guosong Hong[2,3,*]

[1] *Department of Applied Physics, Stanford University, Stanford, California 94305, USA*

[2] *Wu Tsai Neurosciences Institute, Stanford University, Stanford, California 94305, USA*

[3] *Department of Materials Science and Engineering, Stanford University, Stanford, California 94305, USA*

(Received 6 February 2021; revised 31 March 2021; accepted 12 April 2021; published 4 May 2021)

Nanoparticles with a strong absorption of incident radio frequency (rf) or microwave irradiation are desirable for remote hyperthermia treatments. While controversy has surrounded the absorption properties of spherical metallic nanoparticles, other geometries, such as prolate and oblate spheroids, have not received sufficient attention for application in hyperthermia therapies. Here, we use the electrostatic approximation to calculate the relative-absorption ratio of metallic nanoparticles in various biological tissues. We consider a broad parameter space, sweeping across frequencies from 1 MHz to 10 GHz, while also tuning the nanoparticle dimensions from spheres to high-aspect-ratio spheroids approximating nanowires and nanodisks. We find that, while spherical metallic nanoparticles do not offer differential heating in tissue, large absorption cross sections can be obtained from long prolate spheroids, while thin oblate spheroids offer minor potential for absorption. Our results suggest that metallic nanowires should be considered for rf- and microwave-based wireless hyperthermia treatments in many tissues going forward.

DOI: 10.1103/PhysRevApplied.15.054007

I. INTRODUCTION

Radio frequencies (rf) and microwaves are used in the clinic for emerging hyperthermia treatments to destroy cancerous growths in tissues throughout the body [1–3]. Hyperthermia can be applied as a standalone treatment [3], or it can be delivered as an adjuvant therapy in conjunction with chemotherapy [2] and/or radiotherapy [4]. While the high tissue penetration of rf or microwaves enables noninvasive therapies via antenna arrays surrounding the body [2], the achievable spatial focusing is fundamentally limited by the long wavelengths of rf. Thus, others have turned to implantable microwave antennas to minimize off-target heating [1], although this technique is more invasive.

Nanomaterials offer alternative capabilities to "focus" energy delivery in biological systems [Fig. 1(a)] [5,6]. In particular, due to well-established synthesis techniques, tunable localized surface plasmon resonance, and high biocompatibility, gold nanostructures have found widespread use in biomedical applications. Plasmon-resonant gold nanorods are highly efficient at converting near-infrared (NIR) light into heat [8] and have shown promise for the treatment of shallow tumors *in vivo* [9]. Recently, programmable photothermal gene editing was achieved by second near-infrared illumination of a polymer-coated gold nanorod paired with a Cas9 plasmid that was triggered by a heat-inducible promoter [10]. Photothermal techniques are increasingly applied in experimental neuroscience, recently enabling through-scalp stimulation of deep brain regions in mice [11]. Additionally, the rapid heating of spherical gold nanoparticles under 532-nm illumination produces nongenetic photocapacitive stimulation of both cultured neurons and mouse hippocampal slices [12], while gold nanorods conjugated to temperature-sensitive ion channels in the retina endow NIR sensitivity in mice and in postmortem human retinas [13].

Radio frequencies offer deeper tissue penetration than infrared light, but the interaction between metal nanostructures and rf or microwaves is less understood and has been the subject of controversy in recent years [14]. Initially, several studies reported heating of spherical gold nanoparticle suspensions in rf fields [15–19]. However, these reports were contradicted by subsequent experiments, which revealed that Joule heating of the stock solution caused the measured temperature increase of a gold-nanoparticle suspension under rf irradiation [20,21]. Additionally, a theoretical investigation analyzed several classical and quantum absorption mechanisms for metallic nanoparticles and found that no combination of the considered mechanisms could produce the previously reported heating [22]. However, for nanoparticles under 10 nm in diameter, an electrophoretic mechanism was later demonstrated both experimentally [23] and theoretically [24], to account for the observed heating in gold-nanoparticle suspensions. A more recent theoretical work suggested that electrophoretic resonances of small (<5 nm) gold

*guosongh@stanford.edu

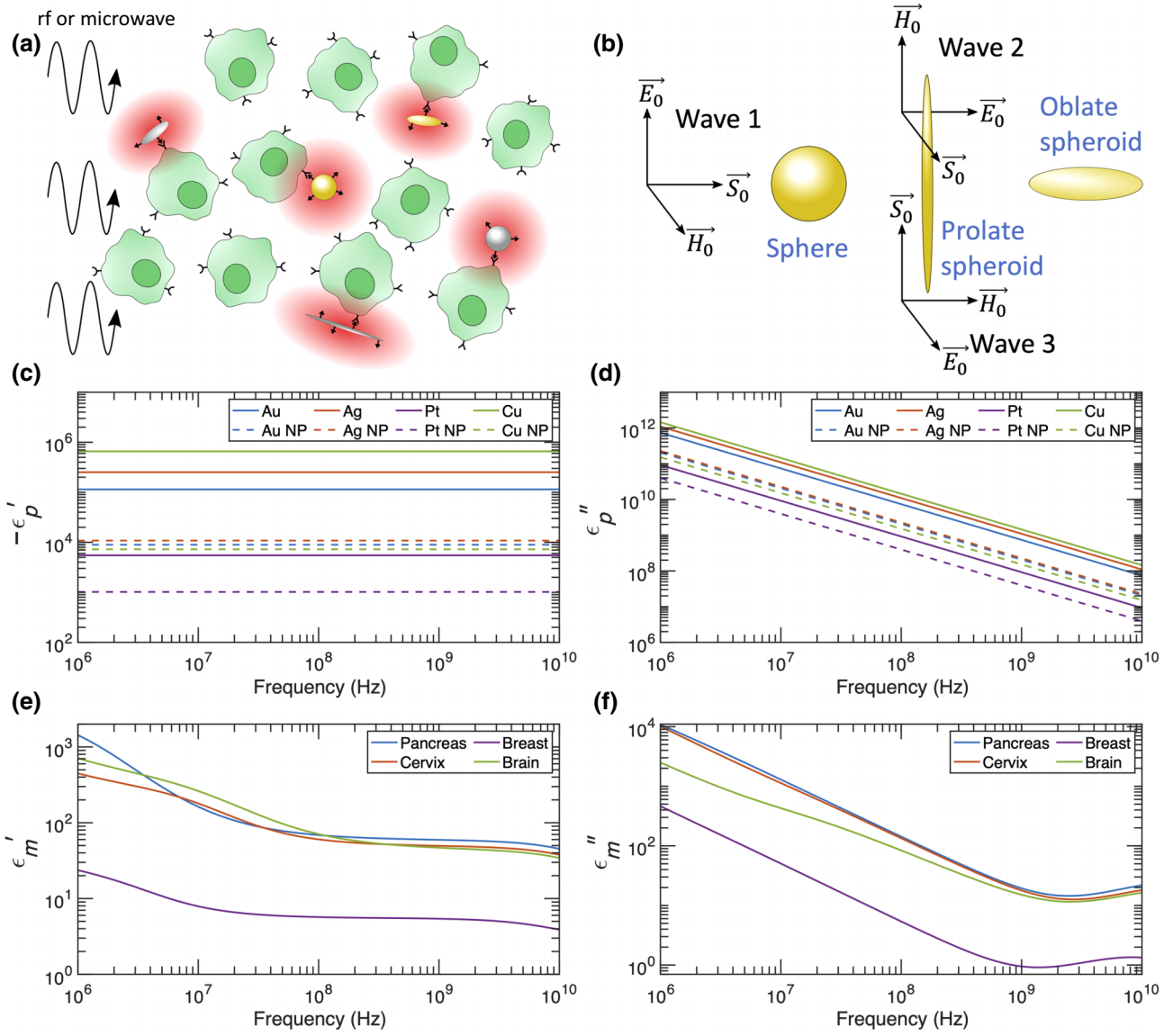

FIG. 1. (a) Schematic of differential heating induced by rf or microwave application to cells targeted by metal nanostructures. (b) Orientation of rf or microwave interactions with nanomaterials. Relative-absorption ratio is averaged over the three propagating waves shown (with equal magnitudes) to account for a collection of randomly oriented spheroids. (c) Negative real component of the dielectric function for metals considered herein. Dashed curves include scattering rate corrections for spherical nanoparticles with 10 nm radius (NP corresponds to nanoparticle). (d) Imaginary component of the dielectric function for metals considered herein. Dashed curves include scattering rate corrections for spherical nanoparticles with 10 nm radius. (e) Real component of the dielectric function for tissues considered herein. Data from Ref. [7]. (f) Imaginary component of the dielectric function for tissues considered herein. Data from Ref. [7].

nanoparticles in the microwave regime would lead to promising differential heating in a weak electrolyte solution [25]. Several key reviews detail the state of the field for heating spherical gold nanoparticles with rf [26,27].

Although opportunities for the rapid heating of spherical metallic nanoparticles with rf appear limited to electrophoretic heating, alternative nanoparticle geometries may offer opportunities for significant differential heating in tissue. A theoretical investigation predicts strong local field enhancements in the near-field zone around carbon nanotubes (CNTs) [28], and differential heating is indeed observed in an experimental report that exposes a tissue-mimicking phantom with CNTs to microwaves [29]. This so-called "lightning-rod effect" is also predicted to occur for elongated ellipsoids [22], and a recent publication has found that the differential heating of silver nanowires under rf increases with increasing aspect ratio, while confirming that spherical silver nanoparticles are not heated under

identical conditions [30]. Another recent work reports that gold nanowires longer than 6 μm absorb microwave radiation [31]. A key theoretical investigation based on the electrostatic approximation [32] derives the absorption cross section for an ellipsoidal particle, followed by numerical examples considering an electrophoretic heating mechanism valid for small nanoparticles [33]. While Joule heating of small spherical gold nanoparticles with rf has been previously discounted [22], the authors of this ellipsoidal investigation do not consider the potential for meaningful Joule heating in larger ellipsoidal particles. The high-aspect-ratio limit of a prolate spheroid is a nanowire [Fig. 1(b)], which is easily synthesized in the laboratory and has recently shown promise for differential heating [30]. Likewise, the high-aspect-ratio limit of an oblate spheroid is a nanodisk [Fig. 1(b)], which may also demonstrate promising absorption characteristics. Furthermore, while most studies investigate spherical nanoparticles on the 1–100 nm length scale, larger particles in the 100 nm–10 μm length scale are still injectable and can be used safely *in vivo* for hyperthermia treatments [34]. Lastly, a study that compares the differential heating of different types of metal nanoparticles in various tissues is missing from the literature, and such a study is important for optimizing hyperthermia treatment protocols.

Here, we present calculations for spherical and spheroidal metal nanoparticles in a variety of tissues that are commonly treated with rf and/or microwave hyperthermia in clinical trials [1,2]. We consider particles ranging in size from nanometers to tens of microns across the frequency spectrum from 1 MHz to 10 GHz, covering the operating frequencies of nearly all hyperthermia treatments [1,2]. This work brings three key advances: first, when considering the electronic response of nanoparticles to incident radiation, we scan over a parameter space of realistic values that can be achieved by synthesizing metal nanostructures with reported methods. Second, we use different types of biological tissue with reported complex dielectric constants for calculating the differential heating of nanoparticles placed therein, instead of an aqueous electrolyte solution as the model for lossy media. Third, our paper proves that metal nanostructures of realistic electrical and geometrical properties can achieve significant differential heating over biological tissues in rf and microwave fields. We hope this theoretical investigation helps to explain previous experimental results, while also suggesting promising particle geometries and frequencies to optimize future hyperthermia protocols.

II. THEORY

After establishing the notational conventions of this manuscript and the methods used to obtain dielectric functions for metallic nanoparticles and biological tissues, we consider the power absorbed by an ellipsoidal particle under the electrostatic approximation, following Refs. [32,33]. We observe that, in the special case of a spherical particle, the result matches the absorption cross section obtained from Mie theory. We conclude with a discussion on the regime of validity of the electrostatic approximation.

A. Conventions

Let μ_0 and ϵ_0 denote the permeability and permittivity of vacuum, respectively; ϵ_p denotes the complex relative permittivity of a metallic particle, and ϵ_m denotes the complex relative permittivity of the surrounding medium. We follow the convention $e^{-i\omega t}$ for time-harmonic fields; thus, the imaginary part of the complex relative permittivity for a passive material is positive: $\epsilon = \epsilon' + i\epsilon''$. The wave number of vacuum is given by $k_0 = (\omega/c_0)$, where c_0 is the speed of light in a vacuum, the complex wave number of a metallic particle is given by $k_p = (\omega/c_0)\sqrt{\epsilon_p}$, and the complex wave number of the surrounding medium is given by $k_m = (\omega/c_0)\sqrt{\epsilon_m}$. We define the complex index of refraction as $n = \sqrt{\epsilon} = n' + in''$. Thus, we have $k_p = (\omega/c_0)(n'_p + in''_p)$ and $k_m = (\omega/c_0)(n'_m + in''_m)$.

B. Dielectric functions of metal nanoparticles and tissue

We calculate the dielectric function of metal nanoparticles using the Drude model for free electrons:

$$\varepsilon_p = 1 - \frac{{\omega_p}^2}{\omega(\omega + i\gamma)}, \tag{1}$$

where ω_p is the plasma frequency and γ is the scattering rate [32]. The Drude model is a good fit to the dielectric function of metals at low frequencies [35], appropriately producing the dc conductivity as $\omega \to 0$ (please see Appendix A for derivation). The plasma frequency, ω_p, is defined as

$${\omega_p}^2 = \frac{Ne^2}{m\epsilon_0}, \tag{2}$$

where N is the number density of free electrons, e is the charge of an electron, and m is the effective mass of an electron [32].

The scattering rate, γ, is dependent on electron scattering from impurities, lattice defects, other electrons, and phonons [36]. In the classical treatment, the scattering rate can be calculated as $\gamma_{\text{bulk}} = v_F/L_\infty$, where v_F is the Fermi velocity and L_∞ is the mean free path in the bulk metal [36]. However, in nanoparticles smaller than the electron mean free path, changes to the scattering rate are required to match experimental measurements of small nanoparticles [37]. The formula for γ can be modified by

introducing a size-dependent term to account for electron scattering from the nanoparticle surface [36,37]:

$$\gamma = \gamma_{\text{bulk}} + \frac{v_F}{L_{\text{eff}}}, \tag{3}$$

where L_{eff} is the effective mean free path. Although there is some disagreement, $L_{\text{eff}} = 4R/3$ is typically used for spherical nanoparticles of radius R [32]. An in-depth analysis relies on geometrical-probability-calculated L_{eff} for spheres, prolate spheroids, and oblate spheroids [36], and we use these relations when calculating the scattering rate, γ, in this manuscript. For a sphere of radius R, the effective mean free path is given by [36]

$$L_{\text{eff}} = 4R/3, \tag{4}$$

matching the typical value reported above. Next, for a prolate spheroid with major axis L (length) and minor axis D (diameter), the effective mean free path is given by [36]

$$L_{\text{eff}} = \frac{2D}{3/2 + 3F_2/2},\ F_2 = \frac{\sin^{-1}(e)}{e},\ e = \sqrt{1-(D/L)^2}. \tag{5}$$

We see that, as we approach the limit of a sphere ($D/L \rightarrow 1$), $F_2 \rightarrow 1$, and thus, $L_{\text{eff}} \rightarrow 4R/3$, as expected. Lastly, for an oblate spheroid with major axis D (diameter) and minor axis T (thickness), the effective mean free path is given by [36]

$$L_{\text{eff}} = \frac{2T}{3/2 + 3F_1/4},\ F_1 = \frac{(1-e^2)}{e}\ln\left(\frac{1+e}{1-e}\right),$$
$$e = \sqrt{1-(T/D)^2}. \tag{6}$$

Once again, in the limit of a spherical particle ($T/D \rightarrow 1$), $F_1 \rightarrow 2$, and thus, $L_{\text{eff}} \rightarrow 4R/3$, as expected.

We apply scattering rate corrections for all particle sizes considered in our analysis, rather than cutting off the correction for particles with $L_{\text{eff}} > L_\infty$, as it is reasonable to assume that particles slightly larger than the bulk mean free path will still host increased scattering rates due to the finite particle size. The correction becomes insignificant for particles with $L_{\text{eff}} \gg L_\infty$, as we would expect from the underlying physics.

We extract the dielectric function, ϵ_m, for different biological tissues across the 1 MHz–10 GHz frequency range from the Gabriel parameterizations [7,38–42]. In particular, we consider the Gabriel parameterizations for pancreatic, cervical, breast, and brain tissue, as these tissues are frequent targets of rf or microwave hyperthermia treatments in clinical trials [1,2]. For brain tissue, we use a gray-matter-to-white-matter ratio of 3:2 [43]. We also consider breast and brain cancerous tissues, with dielectric properties reported in Refs. [44,45]. Although the dielectric properties of some tissues at the cellular scale are heterogeneous and anisotropic [46], a specific challenge of performing simulations at the cellular scale arises from the limited availability of dielectric measurements of the plasma membrane at the frequency range of interest. Therefore, we apply bulk-tissue dielectric measurements throughout this manuscript to increase the tractability of our simulations and the generalizability of our results.

C. Absorption cross section of an ellipsoid

We will consider an ellipsoidal particle placed within a uniform electrostatic field, $\overrightarrow{E_0}$ (see Sec. II D for constraints on the validity of this approximation). Reference [32] solved the problem of an ellipsoidal particle placed in an electrostatic field, $\overrightarrow{E_0}$, applied parallel to the z axis (length of x semiaxis of ellipsoid $= a$, length of y semiaxis of ellipsoid $= b$, length of z semiaxis of ellipsoid $= c$), finding that the electric field, $\overrightarrow{E_1}$, produced within the particle is both constant and parallel to $\overrightarrow{E_0}$. The authors find that the asymptotic perturbing potential induced by the presence of the ellipsoidal particle matches the potential of a dipole with a dipole moment also along the z axis:

$$\vec{p} = V\epsilon_0\epsilon_m \frac{\epsilon_p - \epsilon_m}{\epsilon_m + L_3(\epsilon_p - \epsilon_m)}\overrightarrow{E_0}, \tag{7}$$

where V is the volume of the ellipsoid given by $V = (4\pi/3)abc$, and L_3 is given by

$$L_3 = \frac{3V}{8\pi}\int_0^\infty \frac{dq}{(c^2+q)f(q)}, \tag{8}$$

where $f(q) = \sqrt{(q+a^2)(q+b^2)(q+c^2)}$. On the other hand, the polarizability, α_j, of a particle along any of the three Cartesian axes is defined by [32]

$$\vec{p} = \epsilon_0\epsilon_m\alpha_j\overrightarrow{E_o}. \tag{9}$$

Here, we notice that we can extract the polarizability α_3, which is that in the z direction, by comparing Eqs. (7) and (9). In doing so, we can also generalize our results to an electrostatic field applied along any of the three principal axes, as the z axis we initially choose holds no special properties. We fix the semiaxes to be parallel to the Cartesian axes, given by $\hat{x_i}$ for $i = 1$, 2, and 3. Thus, for an applied electrostatic field, $\overrightarrow{E_0} = E_0\hat{x_i}$, with $i = 1$, 2, or 3, we have

$$\alpha_i = 3V\frac{\epsilon_p - \epsilon_m}{3\epsilon_m + 3L_i(\epsilon_p - \epsilon_m)}, \tag{10}$$

with

$$L_i = \frac{3V}{8\pi}\int_0^\infty \frac{dq}{(a_i^2+q)f(q)}, \tag{11}$$

where $a_1 = a$, $a_2 = b$, and $a_3 = c$ per the definitions given at the beginning of this section. The geometrical factors L_1, L_2, and L_3 sum to one for all ellipsoidal geometries. Next, following the derivation in Ref. [33], we see that the field within the particle $\overrightarrow{E_1}$ is given by

$$\overrightarrow{E_1} = \frac{\epsilon_m \alpha_i}{V(\epsilon_p - \epsilon_m)} \overrightarrow{E_0}. \tag{12}$$

Assuming the particle's dielectric constant is uniform throughout its volume, we can solve for the power loss within the particle using Poynting's theorem:

$$W_{\text{loss}} = \frac{1}{2}\omega\epsilon_0 \text{Im}(\epsilon_p) \int_V |\overrightarrow{E_1}|^2 dV. \tag{13}$$

From Eq. (12), we see that the electric field within the particle is uniform, which simplifies the volume integration:

$$W_{\text{loss}} = \frac{1}{2}\omega\epsilon_0 \text{Im}(\epsilon_p) \frac{1}{V} \frac{|\epsilon_m|^2 |\alpha_i|^2}{|\epsilon_p - \epsilon_m|^2} |E_0|^2. \tag{14}$$

We can arrive at the absorption cross section, C_{abs}, by normalizing W_{loss} by the power density, P, of the incident plane wave:

$$P = \frac{\epsilon_0 c_0}{2} \text{Re}\left(\sqrt{\epsilon_m}\right) |E_0|^2, \tag{15}$$

and thus,

$$C_{\text{abs}} = \frac{k_0}{V} \frac{|\epsilon_m|^2}{\text{Re}\left(\sqrt{\epsilon_m}\right)} \text{Im}(\epsilon_p) \left| \frac{\alpha_i}{\epsilon_p - \epsilon_m} \right|^2. \tag{16}$$

Substitution of α_i and subsequent simplification gives

$$C_{\text{abs}} = \frac{k_0 V}{{L_i}^2} \frac{|\epsilon_m|^2}{\text{Re}\left(\sqrt{\epsilon_m}\right)} \frac{\text{Im}(\epsilon_p)}{|\epsilon_p - \epsilon_m[(L_i - 1)/(L_i)]|^2}. \tag{17}$$

Here, we note that, for the special case of a sphere, $L_i = (1/3)$ for $i = 1$, 2, and 3. Substituting $L_i = (1/3)$ into Eq. (17) for a sphere of radius r, we reach

$$C_{\text{abs}} = 12\pi r^3 k_0 \frac{|\epsilon_m|^2}{\text{Re}\left(\sqrt{\epsilon_m}\right)} \frac{\text{Im}(\epsilon_p)}{|\epsilon_p + 2\epsilon_m|^2}, \tag{18}$$

which matches the absorption cross section for a sphere in an absorbing medium derived in Ref. [24] with an independent approach based on Mie theory.

D. Validity bounds of the electrostatic approximation

The electrostatic approximation offers a useful simplification to calculate absorption cross sections over the broad parameter space covered in the plots discussed below. Rather than relying on computationally expensive numerical techniques, the analytical expressions presented above can easily be evaluated by users in the laboratory or clinic to gain an approximate understanding of the differential heating of a particular combination of frequency, tissue type, and nanoparticle composition, shape, and size. In this section, we consider the physical validity of the electrostatic approximation and review appropriate bounds to govern its application with rf or microwave fields.

Consider an ellipsoidal particle illuminated by a monochromatic plane wave of the form $\vec{E} = E_0 e^{ik_m z - i\omega t}\hat{x}$. At a particular moment in time, the electric field amplitude illuminating the spheroid is given by $E_0 e^{ik_m z}$. If the longest semiaxis of the spheroid (with length a) is oriented along the z direction, then, for $\text{Im}(k_m a) \ll 1$ and $\text{Re}(k_m a) \ll 1$, we have $e^{-ik_m a} \approx e^{ik_m a}$, and thus, the particle is approximately exposed to a uniform field across the volume it occupies. This sets the first condition for the validity of the electrostatic approximation:

$$\frac{\omega}{c_0} n_m' a \ll 1 \text{ and } \frac{\omega}{c_0} n_m'' a \ll 1. \tag{19}$$

Bohren and Huffman showed that the field within an ellipsoidal particle exposed to a uniform electrostatic field aligned with one of its axes was uniform and parallel to the incident field [32]. However, to ensure that the field within the particle is also uniform when exposed to a *plane wave*, we require

$$\frac{\omega}{c_0} n_p'' a \ll 1. \tag{20}$$

Lastly, considering that the field of the incident plane wave changes with a characteristic time of order $\tau = 1/\omega$ and that it takes approximately $\tau^* = a n_p'/c_o$ for signal propagation across the ellipsoid, we desire $\tau^* \ll \tau$ in order for all points within the ellipsoid to simultaneously receive the signal of the changing field. Thus, the final condition for the electrostatic approximation is given by

$$\frac{\omega}{c_0} n_p' a \ll 1. \tag{21}$$

If all of these conditions are met for a given frequency, particle composition, particle size, and medium composition, then the approximation of an electrostatic field that we make in the Sec. II C is valid. In the plots that follow, we define 0.1 as the maximum value that satisfies the condition $\ll 1$.

We note that the use of the electrostatic approximation does not take into account structural features, such as surface or volume inhomogeneities, which could alter the absorption properties of affected nanoparticles. Specifically, polycrystalline metals are less conductive than their single-crystal counterparts due to grain boundaries,

thereby leading to a higher scattering rate, γ; a lower conductivity, σ; and thus, a lower ϵ_p'' [47]. According to Eq. (18), a higher absorption cross section, C_{abs}, and a higher degree of differential heating are expected as a result of polycrystallinity, grain boundaries, and other defects in spherical nanoparticles. The effects of nanoparticle coatings are also beyond the scope of the electrostatic approximation and will not be considered here.

We also note that our analysis, relying on the electrostatic approximation, strictly considers isolated particles and that the absorption properties of nanoparticle aggregates must be treated with different methods. For example, a self-assembled chain of small Au spheres may be approximated with a single prolate spheroid, if the interparticle distance and chemistry affords efficient charge transfer [48–50]. However, more complex numerical simulations are needed for solving the differential heating of these self-assembled nanostructures to account for the different dielectric functions of surface-coating molecules from the conductive particle materials. Specifically, surface-coating molecules are reported as a dielectric layer with low conductivity, thus breaking a single continuous conductive structure into separate dipoles under external fields [51]. This discontinuity in the conductive chain cannot be properly modeled with our analytical method, thereby necessitating numerical simulations.

E. Relative-absorption ratio for randomly oriented particles

Here, we seek to provide appropriate results for *in vivo* conditions. Assuming that no alignment mechanism is present, a large collection of injected or intravenously delivered particles will be randomly oriented. Thus, our quantity of interest is the average absorption cross section, $\langle C_{\text{abs}} \rangle$, which is averaged over all possible particle orientations. Because we choose to work with plane monochromatic waves, we can express an arbitrary field as the superposition of field components that are aligned with our semiaxes. Bohren and Huffman found that the average absorption cross section of an ellipsoid was given by the average of the three absorption cross sections calculated by iteratively assuming that the incident field was parallel to the three particle semiaxes i for $i = 1$, 2, and 3 [32]:

$$\langle C_{\text{abs}} \rangle = \frac{1}{3} \sum_{i=1}^{3} C_{\text{abs}\ i}. \tag{22}$$

While following this approach, we calculate whether the electrostatic approximation is satisfied for each of the three wave directions shown in Fig. 1(b). If a particular semiaxis of a particle violates the electrostatic approximation, we set $C_{\text{abs}\ i} = 0$ for that semiaxis i. Thus, $\langle C_{\text{abs}} \rangle$ calculated in this manuscript is a lower bound on the average absorption cross section, as nanostructures that violate the electrostatic approximation in particular dimensions will still absorb part of the incident radiation, in reality. We justify neglecting more complicated calculations beyond the electrostatic approximation by arguing that field strength decay within large nanoparticles is undesirable, as regions of the nanoparticle exposed to weaker fields will merely act as heat sinks and reduce the particle's differential heating potential. The bounds of the electrostatic approximation given above limit the allowable field decay within nanoparticles, so, by remaining within the bounds of the electrostatic approximation, we can ensure that the entire volume of the nanoparticles under investigation will meaningfully contribute to differential heating.

We use the relative-absorption ratio, F_{abs}, as a measure of differential heating, which is defined here as

$$F_{\text{abs}} = \frac{< C_{\text{abs}} >}{C_{\text{amb}}} = \frac{1}{3} \sum_{i=1}^{3} \frac{1}{L_i^2} \frac{|\epsilon_m|^2}{\text{Im}(\epsilon_m)} \frac{\text{Im}(\epsilon_p)}{|\epsilon_p - \epsilon_m[(L_i - 1)/(L_i)]|^2}, \tag{23}$$

where $C_{\text{amb}} = 2k_0 V \text{Im}(\sqrt{\epsilon_m})$ is the absorption cross section of an identical volume V of the tissue itself. Specifically, differential heating will occur for $F_{\text{abs}} > 1$. By maximizing F_{abs}, the rf or microwave power necessary to achieve hyperthermic temperatures can be minimized, reducing off-target heating of healthy tissues.

III. RESULTS

The negative real part and the imaginary part of the dielectric function for the metals considered here are plotted in Figs. 1(c) and 1(d), respectively. We use the Drude model for free electrons to calculate these curves, relying on the input parameters ω_p and γ. In Appendix B, we discuss the variation in ω_p and γ in the reported literature, and we find that the reported variation does not significantly affect our calculated relative-absorption ratios. The dielectric functions for spherical nanoparticles with $R = 10$ nm are also displayed in Figs. 1(c) and 1(d), which include a correction to the scattering rate based on the effective mean free path [Eq. (3)]. The finite size of these nanoparticles increases the scattering rate, which serves to decrease the magnitude of both ϵ_p' and ϵ_p'' at the low frequencies considered here (please see Appendix A for the low-frequency derivation).

Figures 1(e) and 1(f) show the real and imaginary parts of the dielectric function for the tissues considered here, which is calculated based on parameterizations of Gabriel's measurements [7,38–40]. While the dielectric functions for pancreatic, cervical, and brain tissue are comparable across the 1 MHz–10 GHz spectrum, the dielectric function of the breast is significantly different due to the high lipid content of breast tissue [52,53].

A. Spherical metal nanoparticles do not produce differential heating in rf fields

We begin our analysis by calculating the relative-absorption ratio, F_{abs}, for spherical metallic nanoparticles in rf or microwave fields, a subject of controversy in recent years [14,19,20,22,24]. For the case of a spherical particle, the absorption cross section of an ellipsoid reduces to Eq. (18). In Fig. 2(a), we list parameters that can be tuned when calculating F_{abs}, namely, the frequency (f) of the incident electromagnetic field, the radius (R) of the spherical nanoparticle, the type of metal (determines ϵ_p), and the type of background tissue (determines ϵ_m). We begin by plotting F_{abs} for Au, Ag, Pt, and Cu nanoparticles in the pancreas in Figs. 2(b)–2(e), a common target for hyperthermia therapies in clinical trials. Au, Ag, Pt, and Cu nanoparticles are chosen in this study for their ease of synthesis and surface functionalization, chemical inertness, and many demonstrated applications in biomedicine [54]. By studying Eq. (23) for F_{abs}, we find that, in the case of a sphere ($L_j = 1/3$), assuming $|\epsilon'_p| \gg |\epsilon'_m|$ and $|\epsilon''_p| \gg |\epsilon''_m|$ (valid for all tissues and metals considered here above 10 MHz)

$$F_{\text{abs}} \propto \frac{|\epsilon_m|^2}{|\epsilon_p|^2}\frac{\epsilon''_p}{\epsilon''_m}. \tag{24}$$

Thus, for a fixed nanoparticle material, radius, and frequency, the subsequent differential heating is determined by the ratio of $|\epsilon_m|^2/\epsilon''_m$. The numerator of this ratio dominates due to the squared term, so tissues with smaller $|\epsilon_m|$ will produce weaker differential heating, which explains the smaller F_{abs} for Pt nanoparticles in breast tissue [Fig 2(g)] compared with Pt nanoparticles in the pancreas, cervix, and brain tissue [Figs. 2(d), 2(f), and 2(h)]. Similarly, Au nanoparticles in breast tissue [Fig. 2(i)] produce less differential heating than Au nanoparticles in the pancreas [Fig. 2(b)].

On the other hand, for a fixed tissue type, particle radius, and frequency, the subsequent differential heating relies on the ratio $\epsilon''_p/|\epsilon_p|^2$. Because the denominator dominates in this case, materials with smaller $|\epsilon_p|$ will produce larger F_{abs}. Figures 1(c) and 1(d) show that bulk Pt has the smallest $|\epsilon_p|$ of the four metals considered, suggesting that it will produce the largest F_{abs}. Indeed, we observe that Pt nanoparticles in pancreatic tissue [Fig. 2(d)] produce a larger F_{abs} than Au [Fig. 2(b)], Ag [Fig. 2(c)], or Cu [Fig. 2(e)] nanoparticles. Furthermore, the decrease in $|\epsilon_p|$ caused by the increase in γ for small nanoparticles induces a larger F_{abs}, as seen throughout Fig. 2. That said, even for the optimal combination of small Pt nanoparticles in breast tissue (the lowest considered $|\epsilon_p|$ and highest considered $|\epsilon_m|$), F_{abs} has a maximum value of only about 10^{-3}. This aligns with previous theoretical work

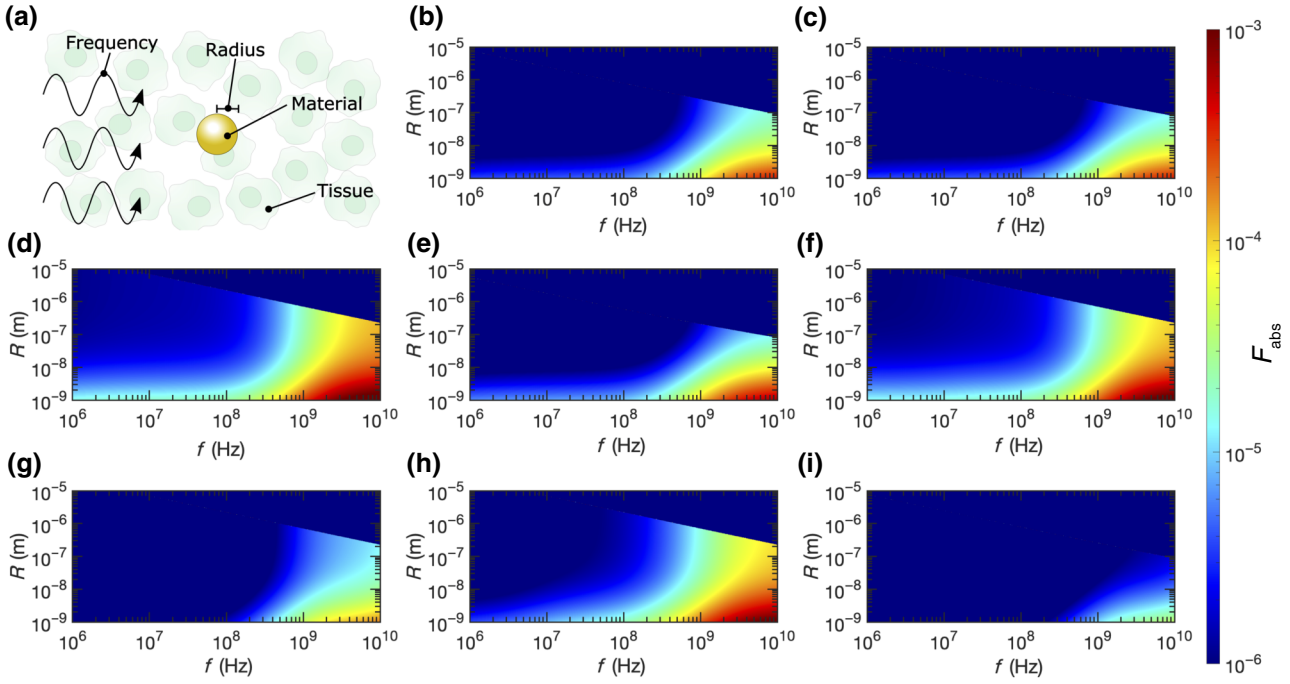

FIG. 2. (a) Labeling the tunable variables in relative-absorption ratio calculations for spherical nanoparticles. (b)–(i) Relative-absorption ratio, F_{abs}, for metallic nanospheres in tissue, as a function of radius (R) and incident electromagnetic wave frequency (f). (b) Pancreas and Au. (c) Pancreas and Ag. (d) Pancreas and Pt. (e) Pancreas and Cu. (f) Cervix and Pt. (g) Breast and Pt. (h) Brain and Pt. (i) Breast and Au. Semiaxes (i.e., radii in the case of spheres) that violate the electrostatic approximation are excluded from all plots; thus, these results represent lower bounds of differential heating.

calculating that Joule heating is insignificant in spherical metal nanoparticles [22].

As discussed in Sec. II E, we do not include contributions to $\langle C_{\rm abs}\rangle$ from ellipsoid axes that violate the electrostatic approximation. Because all three axes have identical dimensions in the case of spherical nanoparticles, $F_{\rm abs}$ abruptly drops to zero above a certain radius determined by f and ϵ_p. Skin-depth effects in these larger nanoparticles will prevent significant heating of the centers of the spheres, effectively producing a heat sink that will limit heating of surrounding tissues.

B. Prolate metal spheroids produce significant differential heating in rf fields

We continue by considering prolate spheroids, which have similar geometries to nanowires in the high-aspect-ratio limit. As for the case of spherical nanoparticles, the tissue type, metal type, and frequency of the incident electromagnetic wave can be tuned, but for prolate spheroids both the diameter (D) and length (L) can be tuned [Fig. 3(a)], adding a geometric degree of freedom compared with spheres. While $C_{\rm abs}$ is identical for all three axes for spherical nanoparticles, we now must consider the contribution to $C_{\rm abs}$ by unique axes for prolate spheroids and average these cross sections to account for a collection of randomly oriented spheroids, according to Eq. (22). Compared with spheres, in the case of prolate or oblate spheroids, it is more challenging to predict promising metals and tissues to maximize $F_{\rm abs}$ based on ϵ_p and ϵ_m because $F_{\rm abs}$ is highly dependent on the values of L_j. This parameter varies widely over the geometrical space we consider in Figs. 3 and 4.

The upper regions of Figs. 3(b), 3(d), 3(f), and 3(h) consider nanowires in the high-aspect-ratio limit in the pancreas, a common target for hyperthermia therapies in clinical trials. Impressively, $F_{\rm abs}$ values up to about 10^7 are attainable for prolate spheroids made of Au or Ag with $D = 10$ nm and $L = 100$ μm in the pancreas. For prolate spheroids with $D = 100$ nm considered in Figs. 3(c), 3(e), and 3(g), we observe smaller values of $F_{\rm abs}$ for the same metals, frequencies, and tissue types. These spheroids have lower aspect ratios than the $D = 10$ nm case, drawing closer to the case of spherical nanoparticles, which show minimal $F_{\rm abs}$.

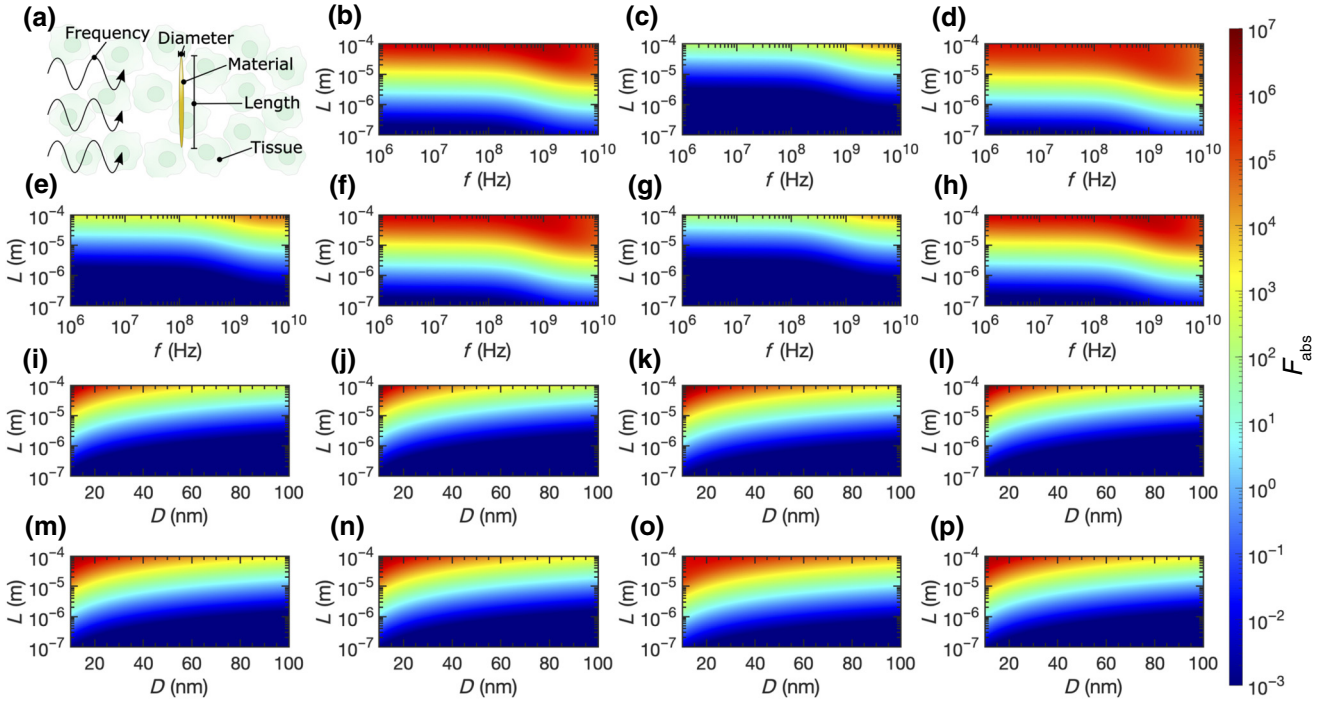

FIG. 3. (a) Labeling the tunable variables in relative-absorption-ratio calculations for prolate spheroids. (b)–(h) Relative-absorption ratio, $F_{\rm abs}$, for metallic prolate spheroids in tissue, as a function of spheroid diameter (D), spheroid length (L), and incident electromagnetic wave frequency (f). (b) Pancreas and Au, $D = 10$ nm. (c) Pancreas and Au, $D = 100$ nm. (d) Pancreas and Pt, $D = 10$ nm. (e) Pancreas and Pt, $D = 100$ nm. (f) Pancreas and Cu, $D = 10$ nm. (g) Pancreas and Cu, $D = 100$ nm. (h) Pancreas and Ag, $D = 10$ nm. (i)–(p) Relative-absorption ratio, $F_{\rm abs}$, for metallic prolate spheroids in tissue at $f = 1$ GHz, as a function of spheroid diameter (D) and spheroid length (L). (i) Breast and Au. (j) Breast and Ag. (k) Breast and Pt. (l) Breast and Cu. (m) Brain and Au. (n) Brain and Ag. (o) Brain and Pt. (p) Brain and Cu. Semiaxes that violate the electrostatic approximation are excluded from all plots; thus, these results represent lower bounds of differential heating.

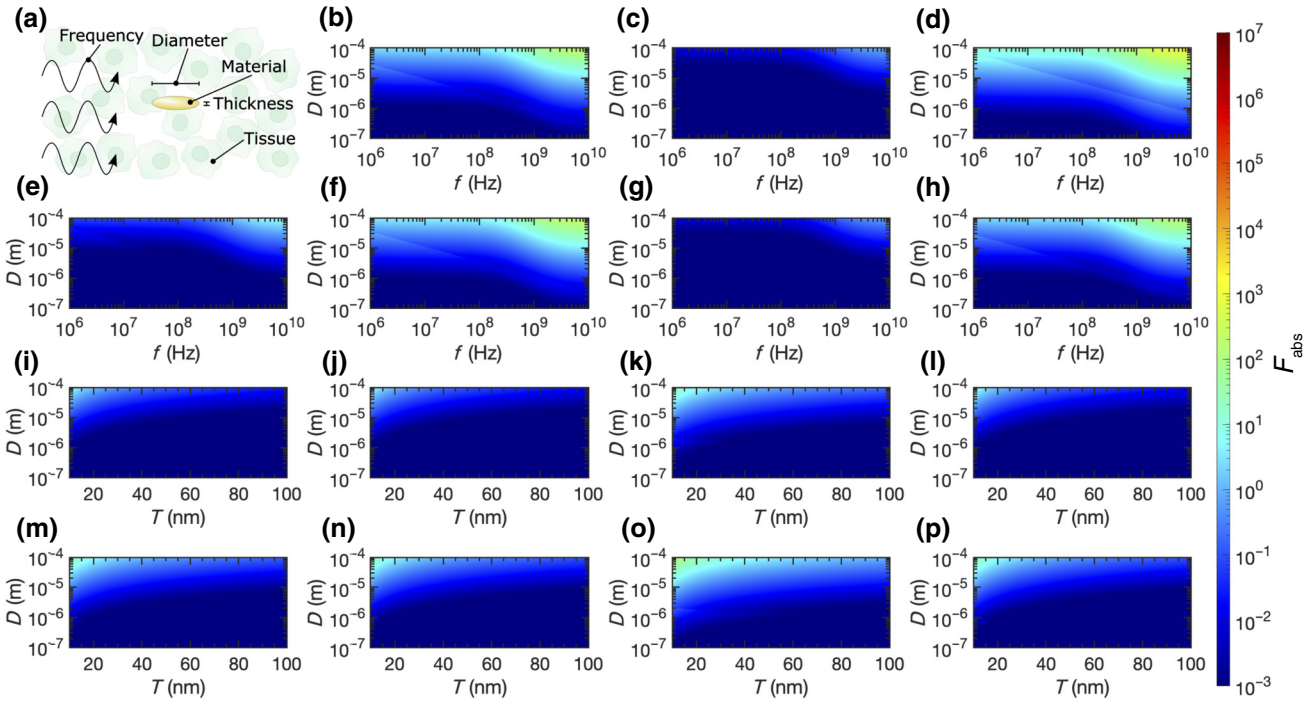

FIG. 4. (a) Labeling the tunable variables in relative-absorption-ratio calculations for oblate spheroids. (b)–(h) Relative-absorption ratio, F_{abs}, for metallic oblate spheroids in tissue, as a function of spheroid diameter (D), spheroid thickness (T), and incident electromagnetic wave frequency (f). (b) Pancreas and Au, $T = 10$ nm. (c) Pancreas and Au, $T = 100$ nm. (d) Pancreas and Pt, $T = 10$ nm. (e) Pancreas and Pt, $T = 100$ nm. (f) Pancreas and Cu, $T = 10$ nm. (g) Pancreas and Cu, $T = 100$ nm. (h) Pancreas and Ag, $T = 10$ nm. (i)–(p) Relative-absorption ratio, F_{abs}, for metallic oblate spheroids in tissue at $f = 1$ GHz, as a function of spheroid diameter (D) and spheroid thickness (T). (i) Breast and Au. (j) Breast and Ag. (k) Breast and Pt. (l) Breast and Cu. (m) Brain and Au. (n) Brain and Ag. (o) Brain and Pt. (p) Brain and Cu. Semiaxes that violate the electrostatic approximation are excluded from all plots; thus, these results represent lower bounds of differential heating.

The preferable differential heating of high-aspect-ratio prolate spheroids is emphasized in Figs. 3(i)–3(p), where it is clear that spheroids with smaller D and larger L produce the largest F_{abs} at 1 GHz. Indeed, the largest values of F_{abs} are obtained in the upper-left corner (smallest D and largest L) for all tissue and metal combinations considered. In this regime, for Pt and Cu spheroids, slightly greater differential heating is obtained in breast tissue compared with brain tissue, while the opposite is observed for spherical Pt nanoparticles in Fig. 2.

Violations of the electrostatic approximation are less obvious in Fig. 3 than in Fig. 2. This is because the largest C_{abs} is obtained when the electric field is aligned with the long axis of the prolate spheroid [$\vec{E_0}$ in wave 1 in Fig. 1(b)]. Since the electric field's amplitude oscillates over the direction of $\vec{S_0}$ in wave 1, the magnitude of the electric field varies minimally over the (small) diameter of the prolate spheroid. Thus, the axis with the largest contribution to $\langle C_{\text{abs}} \rangle$ is unlikely to violate the electrostatic approximation, at least for the range of diameters considered here.

C. Oblate metal spheroids produce moderate differential heating in rf fields

We conclude our analysis by considering the case of oblate spheroids, which we use to approximate nanodisks in the high-aspect-ratio limit. As shown in Fig. 4(a), the diameter (D), thickness (T), and metal type of the oblate spheroids can be tuned, in addition to the tissue type and incident frequency (f). For the plots in Fig. 4, we retain the color bar from Fig. 3 to facilitate a comparison between prolate and oblate spheroids. Similarly to the case of prolate spheroids, we observe larger F_{abs} for higher-aspect-ratio spheroids, as illustrated by the preferable absorption in Figs. 4(b), 4(d), 4(f) and 4(h), with a thickness of 10 nm, compared with Figs. 4(c), 4(e) and 4(g), with a thickness of 100 nm. While differential heating in the pancreas is still attainable with oblate metallic spheroids, the maximum value of F_{abs} for oblate spheroids is about 5 orders of magnitude smaller than the case of prolate spheroids.

In Figs. 4(i)–4(p), we confirm that, at 1 GHz in breast or brain tissue, thin oblate spheroids with large diameters

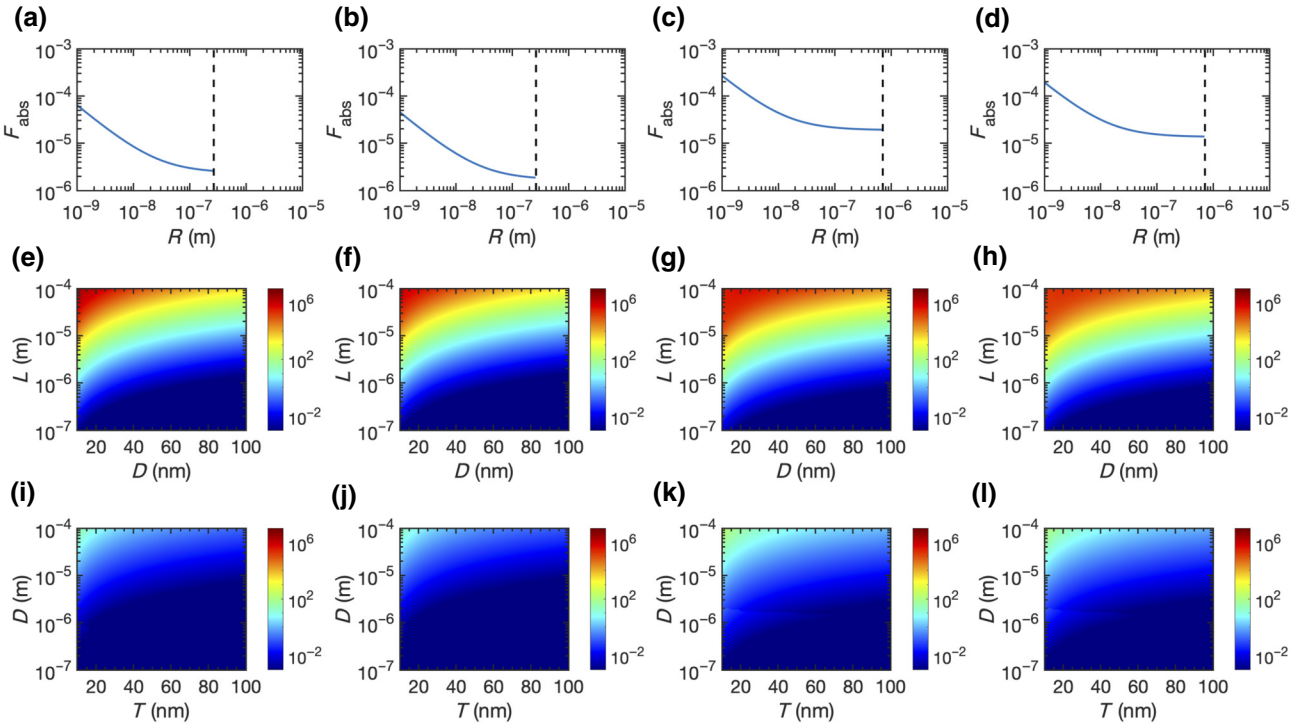

FIG. 5. Relative-absorption ratio for spherical nanoparticles (a)–(d), prolate spheroids (e)–(h), and oblate spheroids (i)–(l) in breast and brain cancerous tissues at 1 GHz. (a), (e), and (i) Brain cancer and Au. (b),(f),(j) Breast cancer and Au. (c),(g),(k) Brain cancer and Pt. (d),(h),(l) Breast cancer and Pt. Dielectric properties of cancerous tissues are taken from Ref. [45] for breast cancer and Ref. [44] for brain cancer. Dashed lines in (a)–(d) represent the boundary of the electrostatic approximation.

are preferable to maximize absorption. Pt spheroids show the largest F_{abs} in both breast and brain tissue, while spheroids of all metals are more absorbing in brain tissue than breast tissue. That said, oblate spheroids perform much worse than prolate spheroids of identical aspect ratio for all metals considered here. Considering the electrostatic approximation, the largest absorption cross sections are contributed to by electric fields aligned with the long axes of oblate spheroids (wave 2 and wave 3) in Fig. 1(b). While wave 2 is likely to violate the electrostatic approximation because the amplitude of $\overrightarrow{E_0}$ in wave 2 varies over the long axis of the spheroid, wave 3 is unlikely to violate the electrostatic approximation because the amplitude of $\overrightarrow{E_0}$ in wave 3 varies over the (small) thickness of the spheroid. Thus, a factor of two in F_{abs} is lost when the electrostatic approximation is violated by wave 2, accounting for the discrete changes in F_{abs} visible in Fig. 4. Although wave 1 is also likely to violate the electrostatic approximation, its contribution to $\langle C_{abs} \rangle$ is less significant, as the electric field is aligned with the short axis of the oblate spheroid.

D. Changes in absorption in cancerous tissues

While the results above are calculated using the dielectric functions of normal tissues, the dielectric functions of some cancerous tissues are reported with larger $|\epsilon_m|$ than their healthy counterparts [44]. Thus, it is useful to calculate F_{abs} in cancerous tissues with reported dielectric functions to check how the relative-absorption ratio changes. It is clear from Eq. (24) that F_{abs} will increase for spherical nanoparticles in cancerous tissues with larger $|\epsilon_m|$. The relationships for prolate and oblate spheroids are less straightforward and depend on the aspect ratio of the nanostructures. In Fig. 5, we calculate F_{abs} for spherical nanoparticles [5(a)–5(d)], prolate spheroids [5(e)–5(h)], and oblate spheroids [Fig. 5(i)–5(l)] at 1 GHz in breast cancer and brain cancer tissues. While we indeed calculate an increase in F_{abs} for spherical nanoparticles, this increase is still not sufficient to achieve differential heating in breast or brain cancer. The trends for prolate and oblate spheroids hold as before, with high-aspect-ratio prolate spheroids offering significant potential for differential heating (maximized by Au in brain cancer with $F_{abs} \approx 1.3 \times 10^6$, slightly lower than $F_{abs} \approx 1.9 \times 10^6$ for Au prolate spheroids in healthy brain tissue), while oblate spheroids offer only minor potential for differential heating in the high-aspect-ratio limit.

IV. DISCUSSION

The results above demonstrate that metallic nanoparticles can indeed be useful transducers of rf or microwave

TABLE I. Relative-absorption ratio of various commercial or reported nanostructures.

Material and geometry	Dimensions	Ref. or vendor	F_{abs} in brain tissue at 1 GHz	F_{abs} in breast tissue at 1 GHz
Ag nanosphere	$D = 20$ nm	Sigma Aldrich	6.3×10^{-6}	1.3×10^{-6}
Au nanosphere	$D = 100$ nm	Nanopartz	3.0×10^{-6}	5.9×10^{-7}
Ag nanowire	$D = 40$ nm, $L = 110$ μm	[56]	1.5×10^{5}	3.3×10^{4}
Cu nanowire	$D = 35$ nm, $L = 200$ μm	[57]	1.6×10^{6}	7.8×10^{5}
Au nanowire	$D = 75$ nm, $L = 10$ μm	Nanopartz	2.0	0.41
Au nanowire	$D = 30$ nm, $L = 6$ μm	Sigma Aldrich	15	3.0
Ag nanodisk	$T = 20$ nm, $D = 530$ nm	[58]	3.6×10^{-4}	7.1×10^{-5}
Pt nanodisk	$T = 20$ nm, $D = 530$ nm	[58]	2.4×10^{-3}	4.8×10^{-4}
Au nanodisk	$T = 20$ nm, $D = 530$ nm	[58]	4.2×10^{-4}	8.2×10^{-5}
Au nanodisk	$T = 35$ nm, $D = 800$ nm	[59]	1.2×10^{-4}	2.4×10^{-5}

radiation into heat for hyperthermia treatments, but the geometry and aspect ratio of the nanoparticles are crucial for determining the degree of heating. While spherical nanoparticles are commonly synthesized in laboratories and are extensively employed in biological applications, the absorption of spherical particles is too low when compared with a background of biological tissue. This result agrees with the theoretical and experimental investigations that rule out Joule heating of spherical gold nanoparticles in rf [20–22].

Prolate spheroids (approximating nanowires) offer powerful differential heating capable of minimizing off-target heating. Nanowires of various metals are also commonly synthesized today, with adjustable diameters and lengths, making them suitable for affordable and tunable hyperthermia treatments [55]. Based on the results of Fig. 3(b)–3(h), it is crucial to employ high-aspect-ratio nanowires to maximize F_{abs}. Similar results are reported experimentally, where silver nanowires of higher aspect ratio demonstrate more powerful heating than low-aspect-ratio nanowires at 13.56 MHz [30,31]. While the length of the longest prolate spheroids considered in Fig. 3 may not be suitable for all *in vivo* applications (e.g., intravenous delivery), nanowires even 1 μm in length offer a factor of 10 increase in C_{abs} over the background tissue, which could still be useful for concentrating heating in hyperthermia treatments.

Oblate spheroids (approximating nanodisks) offer only slight differential heating in tissue, with a maximum F_{abs} of about 10^2. While this degree of differential heating may be suitable for some hyperthermia applications, nanodisks are also less commonly fabricated than nanowires, and thus, the practicality of this geometry may be limited when compared with nanowire-based hyperthermia treatments.

To provide practical guidance for hyperthermia researchers and clinicians, we calculate F_{abs} for various reported or commercially available nanostructures in Table I. Specifically, we calculate F_{abs} for these nanostructures in breast and brain tissue at 1 GHz. We find that none of the spherical nanoparticles nor nanodisks produce differential heating. Commercially available nanowires show minimal promise for differential heating under these conditions (max $F_{abs} \sim 10$), while lab-grown nanowires reported in the literature produce F_{abs} between 10^4 and 10^6. This survey of realistic nanostructures demonstrates the importance of applying high-aspect-ratio nanowires for hyperthermia treatments. While Fig. 4 suggests that high-aspect-ratio nanodisks could also be suitable for differential heating, sufficiently thin and broad nanodisks are not yet demonstrated in the literature, although they may be achievable with lithography and physical vapor deposition. We further guide hyperthermia researchers to the most promising regions of our parameter space in Table II, with high-aspect-ratio prolate spheroids of Cu in breast tissue around 1 GHz offering the largest F_{abs} of the parameter space investigated here. Our theoretical prediction (Table II) agrees with existing experimental observations (Table III): the lack of differential heating of spherical nanoparticles in microwave and rf fields is confirmed in multiple papers [20,21], whereas Ag nanowires only recently demonstrate significant differential heating in a 13.56-MHz electromagnetic field [30]. Our theoretical results in Table II suggest considerable room for improvement by applying 1 GHz microwaves to Cu nanowires, with a diameter of 10 nm and a length of 100 μm, to produce the greatest differential heating.

As an example of the temperature increase that may be expected from realistic nanostructures considered here, we consider a 2-μl bolus injection (typical viral injection volume [60]) of the Cu nanowires reported in Ref. [57] at a volume fraction of 10^{-3}. With $F_{abs} = 1.6 \times 10^6$ for these nanowires (Table I), we expect an effective $F_{abs} = 1.6 \times 10^3$ for the bolus injection. We solve the Pennes bioheat equation (see Appendix C for methods) in brain tissue over 10 s of heating with a 1 GHz field applied at 300 V/m. We select this field strength because it heats noninjected brain tissue by only 0.1 °C over 10 s,

TABLE II. Optimal nanostructures to maximize relative-absorption ratio.

Geometry	Optimal conditions
Spherical particles	Differential heating does not occur under any conditions.
Prolate spheroids	Greatest differential heating occurs around 1 GHz for prolate spheroids made of Cu with $D = 10 - 20$ nm and $L = 100$ μm in breast tissue. Notably, the optimal size parameters are limited by the choice of parameter space in Fig. 3. However, a general trend to maximize F_{abs} holds: a smaller diameter D and a greater length L result in a higher F_{abs} for prolate spheroids composed of any metal in any tissue. In the high-aspect-ratio limit, the optimal frequency f decreases with an increasing length L. F_{abs} is slightly dependent on metal and tissue types, with Cu in breast tissue demonstrating the greatest F_{abs} in the parameter space of interest.
Oblate spheroids	There is minor potential for differential heating between 1 and 10 GHz for oblate spheroids with $T = 10$ nm and $D > 10$ μm. Such nanodisks are not yet demonstrated, but may be attainable with lithography and physical vapor deposition.

TABLE III. Previous experimental reports of hyperthermia with various nanostructures.

Geometry	Experimental reports
Spherical particles	While several initial studies report efficacious heating of spherical nanoparticles [15–19], subsequent experiments suggest that Joule heating of the stock solution, instead of the differential heating of the spherical nanoparticles, is the cause of the temperature increase [20,21]. An electrophoretic mechanism is later demonstrated to account for the temperature increase in suspensions of gold nanoparticles with $D < 10$ nm [23].
Prolate spheroids	Recently, Ref. [30] reports heating of Ag nanowires under rf, with heating rate increasing with aspect ratio (as predicted above). A high rate of cell death is observed for HeLa cancer cells treated with Ag nanowires and rf. The calculations above provide theoretical evidence to spur more experiments with nanowires.
Oblate spheroids	No reports are available in the literature. The calculations above suggest that experiments with high-aspect-ratio nanodisks should be considered.

avoiding damage to surrounding healthy tissue. Meanwhile, the center of the Cu nanowire bolus injection heats by approximately 26 °C over 10 s, providing more than enough heat to induce local tumor-cell death [3].

While much of the literature thus far has focused on spherical gold nanoparticles, the results presented above illuminate the opportunities afforded by alternative geometries and materials. By working within the bounds of the electrostatic approximation, analytical expressions can be used to calculate the relative-absorption ratio across a broad parameter space, minimizing computational cost and enabling straightforward optimization of hyperthermia techniques. Although Joule heating is repeatedly discounted in the case of spherical nanoparticles, this analysis suggests that current flow within nonspherical particles can indeed produce meaningful differential heating. Compared with previous reports that present analytical and numerical solutions of anisotropic nanoparticles to afford maximum differential heating in a lossy medium [28,33], this work is the first to demonstrate the feasibility of rf- or microwave-based remote hyperthermia treatments *in vivo* with realistic metal nanostructures. Furthermore, our results provide a practical guide for choosing the material, size, and geometry of nanoparticles to afford desired local hyperthermia therapy in biological tissues *in vivo* under rf or microwave fields of various frequencies.

V. CONCLUSION

We analytically examine the relative-absorption ratio of metallic nanostructures in biological tissue based on an array of theoretical frames, including classical electromagnetic theory, the Drude model, and the electrostatic approximation. We confirm that spherical nanoparticles do not offer differential heating in tissue, while higher-aspect-ratio geometries, such as nanowires (and, to a lesser extent, nanodisks) offer strong absorption of rf and microwave radiation. Slight differences in the maximum absorption occur, depending on the metal and tissue type considered, but the above calculations can be easily performed in the clinic for optimization, as needed. We believe these results are immediately relevant to hyperthermia treatments, and subsequent work will examine the attainable increase in tissue temperature both around individual nanoparticles and in the bulk volume around a nanoparticle injection, based on the relative-absorption ratios calculated herein.

ACKNOWLEDGMENTS

G.H. acknowledges support from a National Institutes of Health (NIH) Pathway to Independence Award

(National Institute on Aging Grant No. 5R00AG056636-04), a National Science Foundation (NSF) CAREER Award (Grant No. 2045120), a gift from the Spinal Muscular Atrophy (SMA) Foundation, and seed grants from the Wu Tsai Neurosciences Institute and the Bio-X Initiative of Stanford University.

APPENDIX A: CONFIRMING THE VALIDITY OF THE DRUDE MODEL AT LOW FREQUENCIES

Consider the Drude model for free electrons given in Eq. (1). We begin by extracting the real and imaginary parts of the dielectric function:

$$\epsilon' = 1 - \frac{{\omega_p}^2}{\omega^2 + \gamma^2},\ \epsilon'' = \frac{{\omega_p}^2 \gamma}{\omega(\omega^2 + \gamma^2)}. \tag{A1}$$

Taking the low-frequency limit, $\omega \ll \gamma$,

$$\epsilon' \approx 1 - \frac{{\omega_p}^2}{\gamma^2},\ \epsilon'' \approx \frac{{\omega_p}^2}{\omega\gamma}. \tag{A2}$$

In a free-electron model (assuming minimal contribution from bound electrons), $\mathrm{Re}(\sigma) = \epsilon_0 \epsilon'' \omega$ [32], so at low frequencies

$$\mathrm{Re}(\sigma) \approx \frac{\epsilon_0 {\omega_p}^2}{\gamma}. \tag{A3}$$

As $\omega \to 0$ for an applied electric field, the induced current is in phase with the applied field [61], so $\mathrm{Im}(\sigma) \to 0$ and $\sigma = \mathrm{Re}(\sigma) \approx (\epsilon_0 {\omega_p}^2/\gamma)$. Rewriting ω_p using its constituent factors [defined in Eq. (2)] and γ as τ^{-1} where τ is the characteristic scattering time, we obtain

$$\sigma = \frac{Ne^2\tau}{m}. \tag{A4}$$

which matches the definition of the dc conductivity of metals σ_{dc} [61]. Therefore, the Drude model is valid at

TABLE IV. Input parameters for the Drude model from Ref [62].

Metal	ω_p (PHz)	γ_{bulk} (THz)
Au	2.18	6.45
Ag	2.18	4.35
Pt	1.24	16.7
Cu	1.79	2.19

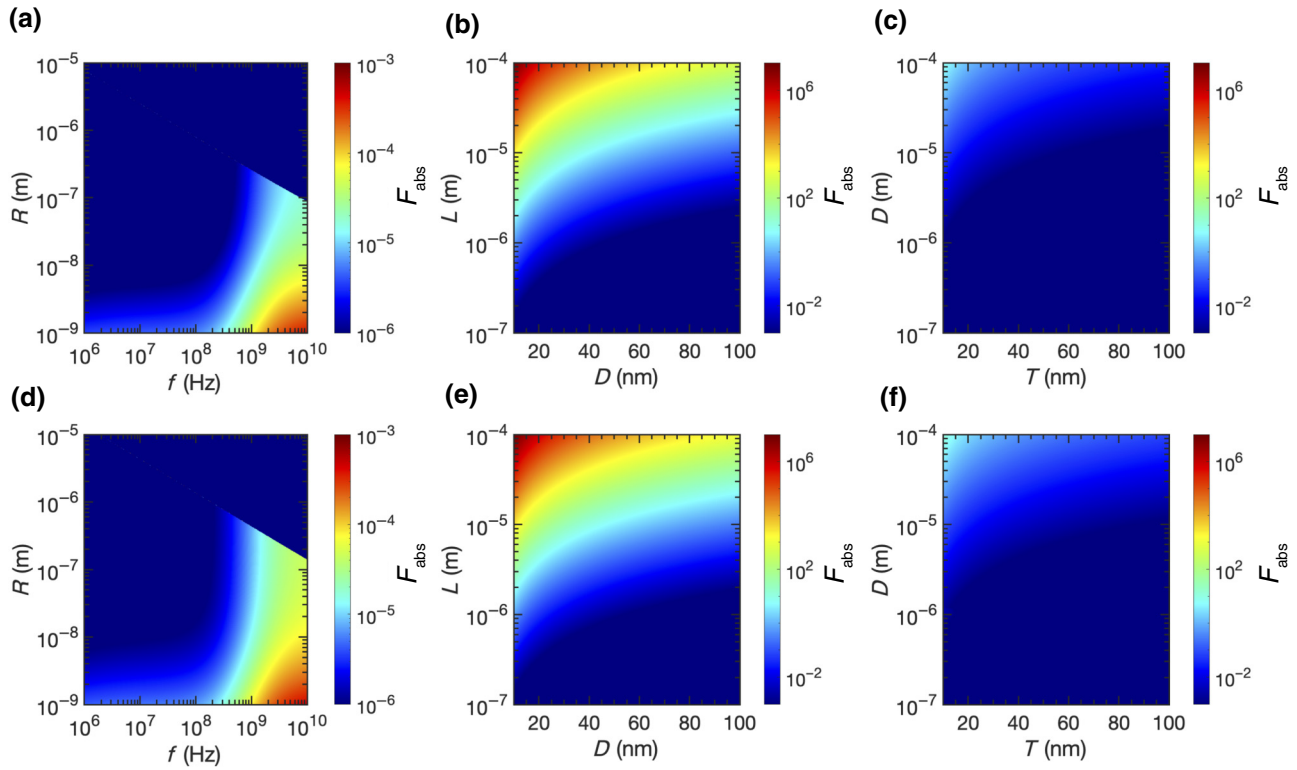

FIG. 6. Lowest (minimum) case of differential heating for spherical gold particles in the pancreas (a), prolate gold spheroids in breast tissue (b), and oblate gold spheroids in breast tissue (c), as obtained by calculations with seven pairs of ω_p and γ_{bulk} reported in Table 1 of Ref. [63]. Highest (maximum) case of differential heating for spherical gold particles in the pancreas (d), prolate gold spheroids in breast tissue (f), and oblate gold spheroids in breast tissue (f), as obtained by calculations with seven pairs of ω_p and γ_{bulk} reported in Table 1 of Ref. [63]. Semiaxes that violate the electrostatic approximation are excluded from all plots.

the low-frequency limit and can thus be applied to rf frequencies. The validity of the Drude model as a good fit to the dielectric function of metals at low frequencies is also experimentally proved [35].

APPENDIX B: CHOICE OF INPUT PARAMETERS FOR THE DRUDE MODEL

To produce Figs. 1–5, we substitute values of the input parameters ω_p and γ_{bulk} reported for Au, Ag, Pt, and Cu in Ref. [62]. We reproduce these values in Table IV for convenience. However, values of ω_p and γ_{bulk} reported in the literature vary, and the choice of these inputs to the Drude model ultimately affect $\langle C_{\text{abs}} \rangle$. For example, Table 1 in Ref. [63] gathers unique sets of ω_p and γ_{bulk} for gold reported in seven different studies.

To confirm the conclusions above, in Fig. 6 we reproduce several key subplots for gold nanostructures from Figs. 2–4, but we display the plots corresponding to the lowest and highest differential heating in the parameter space of interest. For example, Figs. 6(a) and 6(d) cover the same parameter space as Fig. 2(b) for spherical gold nanoparticles in the pancreas. We calculate seven maps of this parameter space, with each map using a unique set of ω_p and γ_{bulk} reported in Ref. [63]. We then determine the lowest and highest cases of differential heating by ranking all seven maps by the maximum F_{abs} occurring within each graph. The lowest-ranking map (minimum differential heating) is shown in Fig. 6(a), and the highest-ranking map (maximum differential heating) is shown in Fig. 6(d). These maps put bounds on the expected absorption properties for spherical gold nanoparticles in the pancreas, as an illustrative case for how variations in input parameters may affect the conclusions of this manuscript. We repeat this process for gold prolate spheroids in breast tissue [covering the parameter space of Fig. 3(i)] in Figs. 6(b) and 6(e) and gold oblate spheroids in breast tissue [covering the parameter space of Fig. 4(i)] in Figs. 6(c) and 6(f). We observe minimal differences between the plots when comparing the minimum and maximum differential heating for spheres, prolate spheroids, and oblate spheroids, suggesting that the variation of reported ω_p and γ_{bulk} in the literature does not significantly affect our conclusions.

APPENDIX C: DIFFERENTIAL HEATING CALCULATIONS

We solve the three-dimensional Pennes bioheat equation in homogenous brain tissue using the bioheatExact function in the k-Wave MATLAB toolbox [64]. Thermal properties of the brain and blood are taken from Ref. [6]. We use a 1 cm^3 cubic domain (designed to approximate the brain of a mouse) with a uniform initial temperature distribution of 37 °C, and a wave with frequency 1 GHz and strength of 300 V/m to minimize heating of surrounding tissues.

[1] C. L. Brace, Microwave tissue ablation: Biophysics, technology, and applications, Crit. Rev. Biomed. Eng. **38**, 65 (2010).

[2] M. M. Paulides, H. Dobsicek Trefna, S. Curto, and D. B. Rodrigues, Recent technological advancements in radiofrequency- and microwave-mediated hyperthermia for enhancing drug delivery, Adv. Drug Deliv. Rev. **163–164**, 3 (2020).

[3] S. Toraya-Brown and S. Fiering, Local tumour hyperthermia as immunotherapy for metastatic cancer, Int. J. Hyperthermia **30**, 531 (2014).

[4] N. R. Datta, S. Rogers, S. G. Ordóñez, E. Puric, and S. Bodis, Hyperthermia and radiotherapy in the management of head and neck cancers: A systematic review and meta-analysis, Int. J. Hyperthermia **32**, 31 (2016).

[5] S. Lal, S. E. Clare, and N. J. Halas, Nanoshell-Enabled photothermal cancer therapy: Impending clinical impact, Acc. Chem. Res. **41**, 1842 (2008).

[6] R. Chen, G. Romero, M. G. Christiansen, A. Mohr, and P. Anikeeva, Wireless magnetothermal deep brain stimulation, Science **347**, 1477 (2015).

[7] D. Andreuccetti, R. Fossi, and C. Petrucci, *An Internet Resource for the Calculation of the Dielectric Properties of Body Tissues in the Frequency Range 10 Hz–100 GHz*, Available from: http://niremf.ifac.cnr.it/tissprop/.

[8] T. B. Huff, L. Tong, Y. Zhao, M. N. Hansen, J.-X. Cheng, and A. Wei, Hyperthermic effects of gold nanorods on tumor cells, Nanomedicine **2**, 125 (2007).

[9] E. B. Dickerson, E. C. Dreaden, X. Huang, I. H. El-Sayed, H. Chu, S. Pushpanketh, J. F. McDonald, and M. A. El-Sayed, Gold nanorod assisted near-infrared plasmonic photothermal therapy (PPTT) of squamous cell carcinoma in mice, Cancer Lett. **269**, 57 (2008).

[10] X. Chen, Y. Chen, H. Xin, T. Wan, and Y. Ping, Near-infrared optogenetic engineering of photothermal nanoCRISPR for programmable genome editing, Proc. Natl Acad. Sci. U.S.A **117**, 2395 (2020).

[11] X. Wu, Y. Jiang, N. J. Rommelfanger, R. Yin, J. Liu, S. Cai, W. Ren, A. Shin, K. S. Ong, K. Pu, and G. Hong, Through-Scalp deep-brain stimulation in tether-free, naturally-behaving mice with widefield NIR-II illumination, bioRxiv 2020.10.21.348037 (2020).

[12] J. L. Carvalho-de-Souza, J. S. Treger, B. Dang, S. B. H. Kent, D. R. Pepperberg, and F. Bezanilla, Photosensitivity of neurons enabled by cell-targeted gold nanoparticles, Neuron **86**, 207 (2015).

[13] D. Nelidova, R. K. Morikawa, C. S. Cowan, Z. Raics, D. Goldblum, H. P. N. Scholl, T. Szikra, A. Szabo, D. Hillier, and B. Roska, Restoring light sensitivity using tunable near-infrared sensors, Science **368**, 1108 (2020).

[14] H. K. Kim, G. W. Hanson, and D. A. Geller, Are gold clusters in RF fields hot or not?, Science **340**, 441 (2013).

[15] S. A. Curley, P. Cherukuri, K. Briggs, C. R. Patra, M. Upton, E. Dolson, and P. Mukherjee, Noninvasive radiofrequency field-induced hyperthermic cytotoxicity in human cancer cells using cetuximab-targeted gold nanoparticles, J. Exp. Ther. Oncol. **7**, 313 (2008).

[16] C. J. Gannon, C. R. Patra, R. Bhattacharya, P. Mukherjee, and S. A. Curley, Intracellular gold nanoparticles enhance non-invasive radiofrequency thermal destruction of human

gastrointestinal cancer cells, J. Nanobiotechnology **6**, 2 (2008).
[17] J. Cardinal, J. R. Klune, E. Chory, G. Jeyabalan, J. S. Kanzius, M. Nalesnik, and D. A. Geller, Noninvasive radiofrequency ablation of cancer targeted by gold nanoparticles, Surgery **144**, 125 (2008).
[18] C. H. Moran, S. M. Wainerdi, T. K. Cherukuri, C. Kittrell, B. J. Wiley, N. W. Nicholas, S. A. Curley, J. S. Kanzius, and P. Cherukuri, Size-dependent joule heating of gold nanoparticles using capacitively coupled radiofrequency fields, Nano Res. **2**, 400 (2009).
[19] K. Hamad-Schifferli, J. J. Schwartz, A. T. Santos, S. Zhang, and J. M. Jacobson, Remote electronic control of DNA hybridization through inductive coupling to an attached metal nanocrystal antenna, Nature **415**, 152 (2002).
[20] D. Li, Y. S. Jung, S. Tan, H. K. Kim, E. Chory, and D. A. Geller, Negligible absorption of radiofrequency radiation by colloidal gold nanoparticles, J. Colloid Interface Sci. **358**, 47 (2011).
[21] X. Liu, H.-J. Chen, X. Chen, C. Parini, and D. Wen, Low frequency heating of gold nanoparticle dispersions for non-invasive thermal therapies, Nanoscale **4**, 3945 (2012).
[22] G. W. Hanson, R. C. Monreal, and S. P. Apell, Electromagnetic absorption mechanisms in metal nanospheres: Bulk and surface effects in radiofrequency-terahertz heating of nanoparticles, J. Appl. Phys. **109**, 124306 (2011).
[23] S. J. Corr, M. Raoof, Y. Mackeyev, S. Phounsavath, M. A. Cheney, B. T. Cisneros, M. Shur, M. Gozin, P. J. McNally, L. J. Wilson, and S. A. Curley, Citrate-capped gold nanoparticle electrophoretic heat production in response to a time-varying radio-frequency electric field, J. Phys. Chem. C **116**, 24380 (2012).
[24] E. Sassaroli, K. C. P. Li, and B. E. O'Neill, Radio frequency absorption in gold nanoparticle suspensions: A phenomenological study, J. Phys. D Appl. Phys. **45**, 075303 (2012).
[25] S. Nordebo, M. Dalarsson, Y. Ivanenko, D. Sjöberg, and R. Bayford, On the physical limitations for radio frequency absorption in gold nanoparticle suspensions, J. Phys. D Appl. Phys. **50**, 155401 (2017).
[26] C. B. Collins, R. S. McCoy, B. J. Ackerson, G. J. Collins, and C. J. Ackerson, Radiofrequency heating pathways for gold nanoparticles, Nanoscale **6**, 8459 (2014).
[27] X. Liu, H.-J. Chen, X. Chen, Y. Alfadhl, J. Yu, and D. Wen, Radiofrequency heating of nanomaterials for cancer treatment: Progress, controversies, and future development, Appl. Phys. Rev **2**, 011103 (2015).
[28] M. V. Shuba, G. Y. Slepyan, S. A. Maksimenko, and G. W. Hanson, Radiofrequency field absorption by carbon nanotubes embedded in a conductive host, J. Appl. Phys. **108**, 114302 (2010).
[29] A. Mashal, B. Sitharaman, X. Li, P. K. Avti, A. V. Sahakian, J. H. Booske, and S. C. Hagness, Toward carbon-nanotube-based theranostic agents for microwave detection and treatment of breast cancer: Enhanced dielectric and heating response of tissue-mimicking materials, IEEE Trans. Biomed. Eng. **57**, 1831 (2010).
[30] X. Liu, H.-J. Chen, R. Xu, and J. Yu, Dispersed silver nanowires enhance radiofrequency heating, IEEE Trans. Nanotechnol. **18**, 279 (2019).
[31] B. P. Khanal and E. R. Zubarev, Gold nanowires from nanorods, Langmuir **36**, 15030 (2020).
[32] C. F. Bohren and D. R. Huffman, *Absorption and Scattering of Light by Small Particles* (John Wiley & Sons, Weinheim, Germany, 1998).
[33] M. Dalarsson, S. Nordebo, D. Sjöberg, and R. Bayford, Absorption and optimal plasmonic resonances for small ellipsoidal particles in lossy media, J. Phys. D Appl. Phys. **50**, 345401 (2017).
[34] D. S. Kohane, Microparticles and nanoparticles for drug delivery, Biotechnol. Bioeng. **96**, 203 (2007).
[35] M. A. Ordal, L. L. Long, R. J. Bell, S. E. Bell, R. R. Bell, R. W. Alexander Jr, and C. A. Ward, Optical properties of the metals Al, Co, Cu, Au, Fe, Pb, Ni, Pd, Pt, Ag, Ti, and W in the infrared and far infrared, Appl. Opt. **22**, 1099 (1983).
[36] E. A. Coronado and G. C. Schatz, Surface plasmon broadening for arbitrary shape nanoparticles: A geometrical probability approach, J. Chem. Phys. **119**, 3926 (2003).
[37] U. Kreibig and L. Genzel, Optical absorption of small metallic particles, Surf. Sci. **156**, 678 (1985).
[38] C. Gabriel, S. Gabriel, and E. Corthout, The dielectric properties of biological tissues: I. literature survey, Phys. Med. Biol. **41**, 2231 (1996).
[39] S. Gabriel, R. W. Lau, and C. Gabriel, The dielectric properties of biological tissues: II. measurements in the frequency range 10 Hz to 20 GHz, Phys. Med. Biol **41**, 2251 (1996).
[40] S. Gabriel, R. W. Lau, and C. Gabriel, The dielectric properties of biological tissues: III. parametric models for the dielectric spectrum of tissues, Phys. Med. Biol. **41**, 2271 (1996).
[41] C. Gabriel, *Compilation of the Dielectric Properties of Body Tissues at RF and Microwave Frequencies, Armstrong Laboratory, Occupational and Environmental Health Directorate* (Radiofrequency Radiation Division, San Antonio, TX, 1996).
[42] K. S. Cole and R. H. Cole, Dispersion and absorption in dielectrics I. Alternating current characteristics, J. Chem. Phys. **9**, 341 (1941).
[43] Y. Ge, R. I. Grossman, J. S. Babb, M. L. Rabin, L. J. Mannon, and D. L. Kolson, Age-related total gray matter and white matter changes in normal adult brain. Part I: Volumetric MR imaging analysis, AJNR Am. J. Neuroradiol. **23**, 1327 (2002).
[44] D.-S. Yoo, The dielectric properties of cancerous tissues in a nude mouse xenograft model, Bioelectromagnetics **25**, 492 (2004).
[45] Y. Cheng and M. Fu, Dielectric properties for Non-invasive detection of normal, benign, and malignant breast tissues using microwave theories, Thorac. Cancer **9**, 459 (2018).
[46] R. Pethig, Dielectric properties of body tissues, Clin. Phys. Physiol. Meas. **8**, 5 (1987).
[47] G. Lormand, Electrical properties of grain boundaries, J. Phys. Colloq. **43**, C6 (1982).
[48] S. Lerch and B. M. Reinhard, Effect of interstitial palladium on plasmon-driven charge transfer in nanoparticle dimers, Nat. Commun. **9**, 1608 (2018).
[49] A. N. Koya and J. Lin, Charge transfer plasmons: Recent theoretical and experimental developments, Appl. Phys. Rev. **4**, 021104 (2017).

[50] K. J. Savage, M. M. Hawkeye, R. Esteban, A. G. Borisov, J. Aizpurua, and J. J. Baumberg, Revealing the quantum regime in tunnelling plasmonics, Nature **491**, 574 (2012).

[51] M. A. Rampi, O. J. A. Schueller, and G. M. Whitesides, Alkanethiol self-assembled monolayers as the dielectric of capacitors with nanoscale thickness, Appl. Phys. Lett. **72**, 1781 (1998).

[52] M. Lazebnik, L. McCartney, D. Popovic, C. B. Watkins, M. J. Lindstrom, J. Harter, S. Sewall, A. Magliocco, J. H. Booske, M. Okoniewski, and S. C. Hagness, A large-scale study of the ultrawideband microwave dielectric properties of normal breast tissue obtained from reduction surgeries, Phys. Med. Biol. **52**, 2637 (2007).

[53] N. K. Pallegar and S. L. Christian, in *Tumor Microenvironment: Non-Hematopoietic Cells*, edited by A. Birbrair (Springer International Publishing, Cham, Switzerland, 2020), pp. 1–13.

[54] R. R. Arvizo, S. Bhattacharyya, R. A. Kudgus, K. Giri, R. Bhattacharya, and P. Mukherjee, Intrinsic therapeutic applications of noble metal nanoparticles: Past, present and future, Chem. Soc. Rev. **41**, 2943 (2012).

[55] S. Lal, J. H. Hafner, N. J. Halas, S. Link, and P. Nordlander, Noble metal nanowires: From plasmon waveguides to passive and active devices, Acc. Chem. Res. **45**, 1887 (2012).

[56] M. J. Saw, B. Ghosh, M. T. Nguyen, K. Jirasattayaporn, S. Kheawhom, N. Shirahata, and T. Yonezawa, High aspect ratio and post-processing free silver nanowires as top electrodes for inverted-structured photodiodes, ACS Omega **4**, 13303 (2019).

[57] S. Ye, A. R. Rathmell, I. E. Stewart, Y.-C. Ha, A. R. Wilson, Z. Chen, and B. J. Wiley, A rapid synthesis of high aspect ratio copper nanowires for high-performance transparent conducting films, Chem. Commun. **50**, 2562 (2014).

[58] C. Langhammer, B. Kasemo, and I. Zorić, Absorption and scattering of light by Pt, Pd, Ag, and Au nanodisks: Absolute cross sections and branching ratios, J. Chem. Phys. **126**, 194702 (2007).

[59] K. Imura, K. Ueno, H. Misawa, H. Okamoto, D. McArthur, B. Hourahine, and F. Papoff, Plasmon modes in single gold nanodiscs, Opt. Express **22**, 12189 (2014).

[60] A. Cetin, S. Komai, M. Eliava, P. H. Seeburg, and P. Osten, Stereotaxic gene delivery in the rodent brain, Nat. Protoc. **1**, 3166 (2006).

[61] M. Dressel and G. Grüner, *Electrodynamics of Solids: Optical Properties of Electrons in Matter* (Cambridge University Press, Cambridge, United Kingdom, 2002).

[62] M. A. Ordal, R. J. Bell, R. W. Alexander Jr, L. L. Long, and M. R. Querry, Optical properties of fourteen metals in the infrared and Far infrared: Al, Co, Cu, Au, Fe, Pb, Mo, Ni, Pd, Pt, Ag, Ti, V, and W, Appl. Opt. **24**, 4493 (1985).

[63] A. Derkachova, K. Kolwas, and I. Demchenko, Dielectric function for gold in plasmonics applications: Size dependence of plasmon resonance frequencies and damping rates for nanospheres, Plasmonics **11**, 941 (2016).

[64] B. E. Treeby and B. T. Cox, K-Wave: MATLAB toolbox for the simulation and reconstruction of photoacoustic wave fields, J. Biomed. Opt. **15**, 021314 (2010).